

Article

Analysis of Thermo-Hydrodynamic Lubrication of Three-Lobe Semi-Floating Ring Bearing Considering Temperature–Viscosity Effect and Static Pressure Flow

Jiwei Dong ¹, Huabing Wen ^{1,*}, Junchao Zhu ¹, Junhua Guo ¹ and Chen Zong ²¹ School of Energy and Power, Jiangsu University of Science and Technology, Zhenjiang 212114, China² Chongqing Jiangjin Shipbuilding Industry Co., Ltd., Chongqing 402260, China; zjydcfzc@163.com

* Correspondence: whb@just.edu.cn; Tel.: +86-139-5289-4094

Abstract: High-power diesel engine turbochargers predominantly utilize floating ring bearings as their primary supporting components. To further enhance their load capacity, multi-lobe noncircular bearings have been progressively employed. This study focuses on the investigation of noncircular three-lobe SFRBs (semi-floating ring-bearing structures) in marine turbochargers. Employing the half-step center Finite Difference Method (FDM) and the Newton–Raphson iterative procedure, the impact of operational parameters such as the journal speed, external load, oil supply pressure, and oil supply temperature on the static and dynamic characteristics of the inner oil film is analyzed. Subsequently, the accuracy of the theoretical model is validated through a comparative analysis of simulation results obtained from Dyrobes and Fluent. The findings indicate that as the oil supply pressure and temperature increase, the temperature rise and maximum oil film pressure of the three-lobe SFRBs gradually decrease, while the oil film thickness progressively increases, thereby significantly improving the lubrication state. The load capacity of the three-lobe SFRBs is primarily sustained by the bottom tile, where wall friction is most likely to occur. Additionally, within the actual speed range, the stiffness and damping of the three-lobe SFRBs exhibit noticeable nonlinear characteristics.

Keywords: three-lobe SFRBs; thermo-hydrodynamic (THD); static performance; dynamic coefficients; operating parameters



Citation: Dong, J.; Wen, H.; Zhu, J.; Guo, J.; Zong, C. Analysis of Thermo-Hydrodynamic Lubrication of Three-Lobe Semi-Floating Ring Bearing Considering Temperature–Viscosity Effect and Static Pressure Flow. *Lubricants* **2024**, *12*, 140. <https://doi.org/10.3390/lubricants12040140>

Received: 18 March 2024

Revised: 4 April 2024

Accepted: 15 April 2024

Published: 18 April 2024



Copyright: © 2024 by the authors. Licensee MDPI, Basel, Switzerland. This article is an open access article distributed under the terms and conditions of the Creative Commons Attribution (CC BY) license (<https://creativecommons.org/licenses/by/4.0/>).

1. Introduction

The turbocharger is a high-speed rotating device installed on an engine, which significantly enhances engine efficiency without compromising the original size and mass of the engine [1]. Due to the propulsion of the hot exhaust gas, the turbocharger operates at a significantly high speed. For example, the speed of marine turbochargers can reach 60,000 rpm, while the more lightweight automotive turbochargers can impressively reach 300,000 rpm [2]. The challenging operating conditions require a rotor-bearing system of outstanding reliability; thus, floating ring bearings are extensively used to support high-speed rotating shafts [3]. At the same time, its dynamic performance and lubrication performance should be carefully designed.

The floating ring bearing is composed of a double-layer fluid film and a floating ring. The floating ring is perforated with small holes to connect the inner and outer oil film, and the oil flows out through both ends [4]. Compared with common single-layer lubricated circular bearings, the floating ring bearing reduces the friction power loss [5] and has better stiffness and damping to suppress vibrations at high speed [6]. Floating ring bearings can be divided into full floating ring bearings (FFRBs) and semi-floating ring bearings (SFRBs) according to the motion form of the ring. The ring of FFRBs can move in a radial direction and rotate around its own axis while the ring of SFRBs is fixed circumferentially by the locating pin and the outer film acts as a squeeze film damper [7]. The disadvantage

of FFRBs is that it has a risk of complete instability, while the SFRBs do not have this problem [8].

FRBs provide better performance; however, the more complex structure undoubtedly increases the difficulty of calculation and analysis, regardless of whether they are FFRBs or SFRBs. Therefore, scholars have extensively studied them over a long period. Orcutt investigated the stability and dynamic load properties of FRBs with specific width-to-diameter ratios and gaps using theoretical and experimental methods [9]. The results indicated that the theoretical design was effective and sufficient for analyzing the rotor-bearing system, except for discrepancies in the stability results. Nikolajsen proposed a theoretical method with linear perturbation to study the stability of journal bearings and FRBs, emphasizing that the influence of viscosity cannot be ignored [10]. Mokhtar calculated the performance of the FRB theoretically based on the infinite length bearing theory with improved boundary conditions and ignored end leakage. The results demonstrated that FRBs had lower friction power loss than fixed sleeve bearings [11]. Li and Rohde [12] analyzed the stability and dynamic characteristics of FRBs based on linear theory and provided stability boundaries. Clarke et al. [13] presented a steady-state model of FRBs that considered thermal effects and assessed its application in the power-generating industry. Andres and his research team conducted comprehensive theoretical and experimental studies on automotive turbochargers, with a specific emphasis on FRB and semi-FRB configurations [14–19]. The research encompassed a linear stability and dynamic characteristic analysis, alongside an investigation into the nonlinear dynamic response of rotor-bearing systems and a thermo-hydrodynamic lubrication analysis. Based on a volume flow model, Duan et al. [20] solved the static and dynamic characteristics using the FDM and perturbation methods, revealing that the dynamic characteristic results from the FDM were closer to the test results than those obtained by the fast Fourier method. Pei et al. [21] studied the effect of surface texture on FRB performance based on the lumped-parameter thermal model, demonstrating that surface texture significantly affected the static characteristics of the FRB. Wang et al. [22] established a model for magnetorheological fluids lubrication in FRBs and SFRBs, indicating that bearing damping could be altered by changing the magnetic field, which could be further utilized to suppress vibration. Guo et al. [23] established a simulation model considering the temperature–viscosity effect and solved the dynamic characteristic coefficient of FRBs using the FDM and force balance. The results revealed that the temperature–viscosity effect reduced the ring speed ratio and stability of FRBs. Zhang et al. [24] established an analytical model to predict the thermodynamic performance of FRBs with a circumferential oil tank then solved the Reynolds equation by using the separation-of-variable method and compared it with the FDM to analyze the lubrication performance under different oil supply conditions. Dyk et al. [25] thoroughly analyzed several different linearization methods of FRBs and compared them with the simulated response of nonlinear rotor-bearing systems, proving the effectiveness and low computational cost of the linear analysis method. Shuai et al. [26] established a thermal fluid model for FRBs with deep and shallow cavities and analyzed the influence of laminar flow and turbulence on stability. Ziese et al. [27] adopted the Reynolds equation with mass-conserving cavitation according to the two-phase model to analyze the influence of cavitation on the performance of SFRBs. Based on the written simulation program, Xie and Zhu [28] calculated the static and dynamic characteristics of FRBs considering various coupling factors in a comprehensive and detailed manner. Historically, these studies primarily focused on common circular FRBs and less on noncircular shapes. Below are several recently published papers. Soni and Vakharia [29,30] analyzed the static and dynamic characteristics of FRBs with elliptical two lobes using the finite element method, concluding that both were noticeably superior to circular FRBs. Zhang et al. [31,32] also investigated this structure as well as FRBs with three lobes. Nonlinear simulation results demonstrated that the FRB with an elliptical ring and bushing could suppress sub-synchronous vibration, while the three-lobe FRB with a high preload factor could completely suppress it.

In summary, the lubrication characteristics of noncircular multi-lobe SFRBs have received limited attention from scholars. These SFRBs constitute a system with interconnected inner and outer oil films, and the impact of outer oil film static pressure on the lubrication state of the inner film remains unclear. This paper focuses on the noncircular three-lobe SFRBs used in marine turbochargers. Considering the temperature–viscosity effect of lubricating oil and the static pressure of the outer oil film, we formulated lubrication equations, thermal balance equations, load equations, and equations governing stiffness and damping for the three-lobe SFRBs. Employing the half-step center FDM and the Newton–Raphson iterative procedure, we analyzed the effects of operational parameters such as journal speed, external load, oil supply pressure, and oil supply temperature on the static and dynamic characteristics of the inner oil film (Appendix A). Finally, we validated the accuracy of our theoretical model by comparing simulation results obtained from Dyrobes and Fluent. The resulting conclusions have significant guiding implications for the design of multi-lobe SFRBs in turbochargers.

2. Theoretical

2.1. Physical Model

The structure of the SFRB on a turbocharger in this study is illustrated in Figure 1a below. The blue structures in the figure represent the floating ring and bushing, while the yellow structures depict the oil film. It is noteworthy that the inner oil film depicted here only represents the dynamic pressure oil film. Additionally, the oil film rupture boundary on the three tiles is defined by the Reynolds boundary, which implies that it is positioned at an angle behind the eccentric line. The inner wall of the floating ring is equipped with three oil grooves, with each groove positioned at a 14° angle relative to the bearing center. The grooves are treated as hydrostatic chambers in this paper, and the oil film at the grooves is the hydrostatic oil film and its pressure is the oil supply pressure. The floating ring features three holes and three grooves, among which the grooves are designed to accommodate locating pins, thereby preventing the floating ring from rotating. However, radial fretting occurs on the floating ring due to the clearance of the grooves being much larger than that of the outer film. During a transient dynamic analysis of the rotor-bearing system, the outer film with motion caused by squeeze can be considered as a damper. Conversely, in a static analysis, the calculation of the outer oil film force can be disregarded. Furthermore, since the rotation of the journal forms a dynamic pressure oil film on each lobe, the balance of the inner oil film force should be considered.

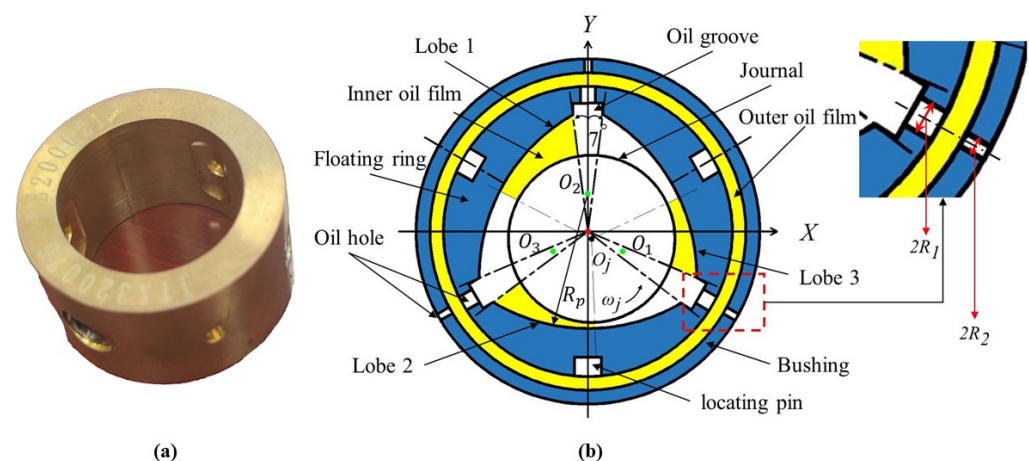


Figure 1. Physical model of three-lobe SFRBs. (a) Actual photograph of three-lobe SFRBs; (b) schematic diagram of three-lobe SFRBs.

2.2. Mathematical Model

2.2.1. Dynamic Pressure Equation

The inner film of the SFRBs is composed of three dynamic pressure oil films distributed on three lobes; therefore, the pressure distribution needs to be calculated separately on each lobe. The dynamic pressure is determined by an incompressible steady-state Reynolds equation, whose expression in cylindrical coordinates is as follows:

$$\frac{\partial}{R_j^2 \partial \varphi} \left(\frac{\rho h_\alpha^3}{12\mu} \frac{\partial P_\alpha}{\partial \varphi} \right) + \frac{\partial}{\partial z} \left(\frac{\rho h_\alpha^3}{12\mu} \frac{\partial P_\alpha}{\partial z} \right) = \frac{U_j}{2} \frac{\partial \rho h_\alpha}{R_j \partial \varphi} \tag{1}$$

where R_j is the radius of the journal; U_j is the journal linear velocity; P and h are the dynamic pressure and thickness of the oil film, respectively; subscript $\alpha = 1, 2, 3$ represents the corresponding lobe sequence number, which can be seen in Figure 1b; φ is the angle in the circumferential direction, and the range of it from the edge of each lobe to the termination edge along the rotation direction; and ρ and μ are the density and dynamic viscosity, respectively.

2.2.2. Thickness Equation

Based on the bearing geometry, it is necessary to calculate the film thickness on three lobes separately. The schematic diagram of the angle calculation is shown in Figure 2a. In Figure 2a, $O_1, O_2,$ and O_3 are the centers of the three lobes, respectively; e represents the eccentricity; and θ and δ represent the attitude angle and pre-eccentricity, respectively. And then, the relations describing them can be written as follows:

$$h_\alpha = C_p(1 + \varepsilon_\alpha \cos(\varphi - \theta_\alpha)) \tag{2}$$

$$\varepsilon_\alpha = \sqrt{\varepsilon^2 + m^2 - 2\varepsilon m \cos \left[\varphi - \frac{\pi(2 - \alpha)}{3} \right]} \tag{3}$$

$$\theta_1 = \frac{4\pi}{3} + \arcsin \frac{\varepsilon \sin \left[\varphi - \frac{\pi}{3} \right]}{\varepsilon_1}$$

$$\theta_2 = \arcsin \frac{\varepsilon \sin \varphi}{\varepsilon_2} \tag{4}$$

$$\theta_3 = \frac{2\pi}{3} - \arcsin \frac{\varepsilon \sin \left[\varphi + \frac{\pi}{3} \right]}{\varepsilon_3}$$

where ε_α is the eccentricity of each lobe, $\varepsilon = e/C_p$ is the eccentricity ratio of the journal center relative to the bearing center, $C_p = R_p - R_j$; θ_α is the attitude angle of each lobe, and m is the preload factor for the bearing.

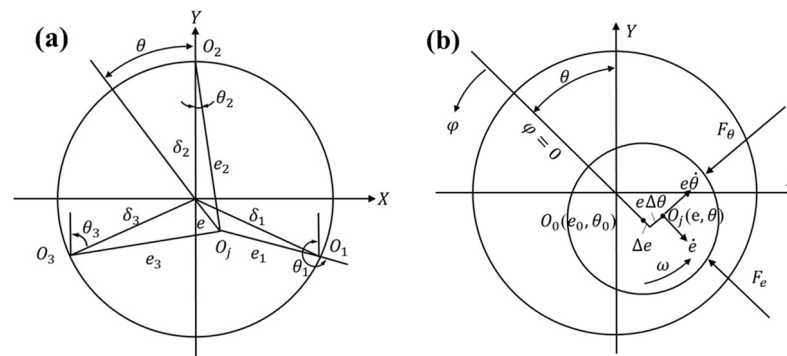


Figure 2. Schematic diagram of oil film thickness and dynamic characteristics. (a) Angle calculation of inner film thickness; (b) coordinate system of dynamic coefficients calculation.

2.2.3. Thermal Equation

During stable operation, heat is mainly generated by the inner oil film, and the function of the outer oil film is to provide lubricating oil and optimize heat dissipation. The provided lubricating oil flows into oil grooves from the inlet on the floating ring and then flows on each lobe; ultimately, it flows out from the lobe end and takes away heat simultaneously. This function is manifested in calculations of the static pressure flow. The lumped-parameter thermal model has the advantages of high computational efficiency and accuracy when calculating the steady-state oil film temperature, and its core idea is to ignore all unsteady heat flow terms. This method is adopted in the thermal calculation in this paper for the three-lobe SFRBs. The heat balance equation of the three-lobe SFRBs is as follows:

$$c_p \rho Q_i \Delta T_i + A_i H_i (\Delta T_i - \Delta T_r) = P_f \quad (5)$$

$$c_p \rho Q_o \Delta T_o + A_o H_o (\Delta T_r - \Delta T_o) = 0 \quad (6)$$

$$A_i H_i (\Delta T_i - \Delta T_r) + A_o H_o (\Delta T_o - \Delta T_r) = 0 \quad (7)$$

where Q represents the total flow rates of the bearing; the subscripts I , o , and r represent the inner and outer oil film and floating ring, respectively; c_p is the specific heat capacity of the oil; ΔT is the temperature rise relative to the oil supply temperature; A corresponds to the heat transfer area; and H denotes the heat transfer coefficient, and its computing method can be found by referring to the literature [33].

The viscosity of the oil changes with the oil temperature and the relationship between them can be described by the Vogel model as follows:

$$\mu = \mu_0 \exp\left(\frac{b}{c + T}\right) \quad (8)$$

The coefficients of the model are obtained by fitting the actual viscosity data of the CD40 oil, and the fitting curve is shown in Figure 3. The values of the coefficients are as follows: $\mu_0 = 6.671 \times 10^{-7}$, $b = 2504.96$, and $c = 173.15$.

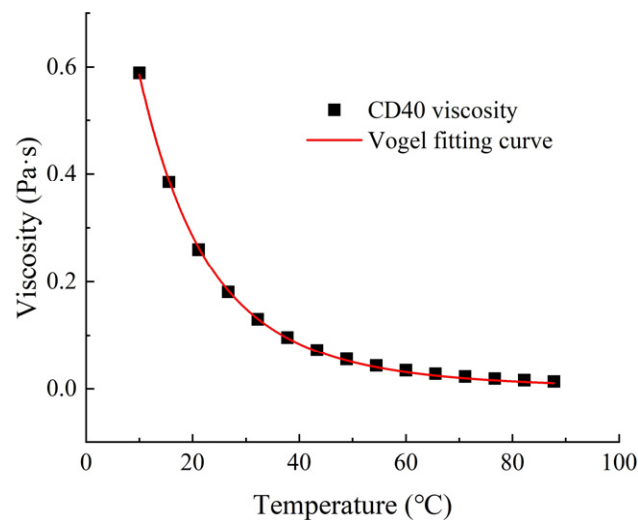


Figure 3. Temperature–viscosity curve of CD40 oil.

2.2.4. Static Characteristic Parameters

Under a quasi-steady state, the power loss of the inner film can be obtained by integrating the simplified energy equation. And, the expression is as follows:

$$W = \sum_{\alpha=1}^3 \int_0^L \int_{\varphi_{\alpha}}^{\varphi_{\alpha}+\beta} \left\{ \frac{h_{\alpha}^3}{2} \left[\left(\frac{\partial P_{\alpha}}{\partial x} \right)^2 + \left(\frac{\partial P_{\alpha}}{\partial y} \right)^2 \right] + \frac{\mu_i}{h_{\alpha}} \omega^2 R_j^2 \right\} R_j d\varphi dz \quad (9)$$

It is worth noting that the calculation of the inner film flow rate Q_i reflects on two parts, one is the end leakage caused by the dynamic pressure and the other one is the flow rate caused by the static pressure of the oil supply. The end leakage of the outer oil film is only induced by static pressure. The expressions are as follows:

$$Q_i = Q_{i1} + Q_{i2} \quad (10)$$

$$Q_{i1} = 2 \sum_{\alpha=1}^3 \int_{\varphi_{\alpha}}^{\varphi_{\alpha}+\beta} \left[-\frac{h_{\alpha}^3}{12\mu} \frac{\partial P_{\alpha}}{\partial z} \right]_{z=L_i} R_j d\varphi \quad (11)$$

where the subscripts 1 and 2 represent the flow rate caused by dynamic and static pressure, respectively.

The flow rate calculated by Equation (11) is derived from the dynamic pressure gradient solved by the Reynolds equation, and the static pressure flow rate is calculated in the following way. Moreover, the two of them are calculated separately. Firstly, the lubricating oil of the inner and outer oil film flows into the oil inlet on the floating ring and bushing individually and flows out at both ends. The oil at the inlet and outlet satisfies the Bernoulli equation of the viscous fluid's total flow, which can be described as follows:

$$P_s + \frac{1}{2}\rho v_{si}^2 + \rho g H_{si} = P_i + \frac{1}{2}\rho v_i^2 + \rho g H_i + h_{wi} \quad (12)$$

$$P_s + \frac{1}{2}\rho v_{so}^2 + \rho g H_{so} = P_o + \frac{1}{2}\rho v_o^2 + \rho g H_o + h_{wo} \quad (13)$$

where v_{si} and v_{so} represent the velocity of the flow at the inlet of the floating ring and bushing, respectively, and h_{wi} and h_{wo} are the pressure loss of the inner and outer oil film, respectively; their calculations can be described by the Darcy–Weisbach equation. Moreover, the shape of clearance can approximately be a narrow circular annulus. And, h_w can be described by $h_w = \lambda_p \frac{L}{2C_b} \frac{\rho v^2}{2}$. Through calculations, it is found that h_w can be ignored. Additionally, the lubricating oil satisfies the flow continuity equation at the inlet and outlet: $v_i A_i = v_{si} A_{si}$, $v_o A_o = v_{so} A_{so}$; A_{si} and A_{so} stand for the area of the inlet on the floating ring and bushing, respectively, and $A_{si} = N_1 \cdot \pi R_1^2$ and $A_{so} = N_2 \cdot \pi R_2^2$, N_1 , and N_2 are the number of oil inlets. Without considering the journal tilt, $H_{si} = H_i$ and $H_{so} = H_o$, so the velocity of flow at the ends of the inner and outer oil film can be calculated:

$$v_i = \sqrt{\frac{2 \cdot P_s}{\rho} \cdot \frac{1}{\left(1 - \frac{A_i^2}{A_{si}^2}\right)}} \quad (14)$$

$$v_o = \sqrt{\frac{2 \cdot P_s}{\rho} \cdot \frac{1}{\left(1 - \frac{A_o^2}{A_{so}^2}\right)}} \quad (15)$$

Therefore, the static pressure flow of the inner film Q_{i2} and outer film Q_o can be obtained: $Q_{i2} = v_i A_i$, $Q_o = v_o A_o$.

After the dynamic pressure distribution of the inner film on each lobe was obtained by solving Equations (1)–(4), we integrated the dynamic pressure of each lobe along the calculation domain, respectively, and then synthesized them into two directions x and y to obtain the load capacity:

$$F_x = \sum_{\alpha=1}^3 \int_0^l \int_{\varphi_{\alpha}}^{\varphi_{\alpha}+\beta} P_{\alpha} \sin R_j d\varphi dz \quad (16)$$

$$F_y = \sum_{\alpha=1}^3 \int_0^l \int_{\varphi_{\alpha}}^{\varphi_{\alpha}+\beta} P_{\alpha} \cos R_j d\varphi dz \quad (17)$$

At a steady state, the journal meets the force balance; that is, $F = Fg$. If the balance equation is not satisfied, the eccentricity ratio will be adjusted by a bisection, and the attitude angle will be adjusted by the following method:

$$\theta_{new} = \theta_{old} - \arctan \frac{F_x}{F_y} \quad (18)$$

2.2.5. Dynamic Coefficients

The small perturbation method is an effective method to solve the dynamic characteristics. When the bearing reaches the steady state, the stiffness and damping coefficients can be received by applying velocity and displacement perturbation to the journal. The stiffness and damping of the three lobes were calculated individually, and the total stiffness and damping of the inner oil film were obtained by synthesizing them. The schematic diagram of the calculation is shown in Figure 2b. The expressions under $e - \theta$ coordinates on each lobe are as follows:

$$\begin{cases} K_{ee} = -\int_0^L \int_{\varphi_\alpha}^{\varphi_\alpha+\beta} P_e \cos \varphi R_j d\varphi dz \\ K_{e\theta} = -\int_0^L \int_{\varphi_\alpha}^{\varphi_\alpha+\beta} P_\theta \cos \varphi R_j d\varphi dz \\ K_{\theta\theta} = \int_0^L \int_{\varphi_\alpha}^{\varphi_\alpha+\beta} P_\theta \sin \varphi R_j d\varphi dz \\ K_{\theta e} = \int_0^L \int_{\varphi_\alpha}^{\varphi_\alpha+\beta} P_e \sin \varphi R_j d\varphi dz \end{cases} \quad (19)$$

$$\begin{cases} C_{ee} = -\int_0^L \int_{\varphi_\alpha}^{\varphi_\alpha+\beta} P'_e \cos \varphi R_j d\varphi dz \\ C_{e\theta} = -\int_0^L \int_{\varphi_\alpha}^{\varphi_\alpha+\beta} P'_\theta \cos \varphi R_j d\varphi dz \\ C_{\theta\theta} = \int_0^L \int_{\varphi_\alpha}^{\varphi_\alpha+\beta} P'_\theta \sin \varphi R_j d\varphi dz \\ C_{\theta e} = \int_0^L \int_{\varphi_\alpha}^{\varphi_\alpha+\beta} P'_e \sin \varphi R_j d\varphi dz \end{cases} \quad (20)$$

In order to obtain the stiffness and damping coefficient in the cartesian coordinate system, both sides of the results in the $e - \theta$ coordinates can be multiplied by the transformation matrix, and their transformation relationship is shown as follows:

$$\begin{bmatrix} K_{xx} & K_{xy} \\ K_{yx} & K_{yy} \end{bmatrix} = \begin{bmatrix} \cos \varphi & -\sin \varphi \\ \sin \varphi & \cos \varphi \end{bmatrix} \cdot \begin{bmatrix} K_{ee} & K_{e\theta} \\ K_{\theta e} & K_{\theta\theta} \end{bmatrix} \cdot \begin{bmatrix} \cos \varphi & \sin \varphi \\ -\sin \varphi & \cos \varphi \end{bmatrix} \quad (21)$$

$$\begin{bmatrix} C_{xx} & C_{xy} \\ C_{yx} & C_{yy} \end{bmatrix} = \begin{bmatrix} \cos \varphi & -\sin \varphi \\ \sin \varphi & \cos \varphi \end{bmatrix} \cdot \begin{bmatrix} C_{ee} & C_{e\theta} \\ C_{\theta e} & C_{\theta\theta} \end{bmatrix} \cdot \begin{bmatrix} \cos \varphi & \sin \varphi \\ -\sin \varphi & \cos \varphi \end{bmatrix} \quad (22)$$

2.2.6. Boundary Conditions

Reynolds boundary conditions are used in this paper, where φ' is the initial angle of oil film rupture on each lobe:

$$\begin{cases} P|_{z=\pm 1} = 0 \\ P|\varphi = \varphi_\alpha = 0, P|\varphi = \varphi' = 0 \\ \frac{\partial P}{\partial \varphi}|\varphi = \varphi' = 0 \end{cases} \quad (23)$$

3. Procedure and Verification

3.1. The Solution Procedure

The flowchart outlining the numerical calculation process for three-lobe SFRBs is depicted in Figure 4. Prior to commencing the calculation, it is imperative to establish parameters pertaining to both the structure and lubricating oil. Once the oil supply pressure and temperature are determined, the side flow rate of the inner and outer film can be computed using Equations (10)–(15). The calculated static pressure flow rate is subsequently integrated into the thermal balance calculation, which is accomplished through iteration. At the outset of each iteration loop, it is essential to make an assumption regarding the temperature rise of the floating ring and then initialize the temperature rise of the inner and

outer film. For practicality, the ambient temperature suffices. Viscosity is determined based on the oil temperature rise in each iteration loop according to the temperature–viscosity curve. During steady-state calculations, the outer oil film of SFRBs can be computed without accounting for the equilibrium position of the floating ring, and the outer oil film is solely utilized for thermodynamic heat transfer analysis. Simultaneous consideration must be given to journal motion and heat transfer for the inner film. In computing the inner oil film, the eccentricity ratio and attitude angle of the journal are initially assumed, and the pressure distribution is derived by solving the Reynolds equation of each lobe using the FDM. Convergence is accelerated through successive over-relaxation. The load capacity is determined by the Simpson integral for the pressure distribution of each of the three lobes, and the balance between the total bearing capacity of the oil film and the external load is established. Subsequent to load balancing, the friction power loss and end leakage of the inner film can be computed. Furthermore, the temperature rise in the inner and outer film as well as the floating ring can be derived from Equations (5)–(7). However, if the calculated temperature rise of the floating ring deviates from the assumed value, the corrected method utilizing the Newton–Raphson iteration is employed until the temperature rise in the floating ring meets the convergence criterion. The convergence criteria for the oil film pressure, oil film load capacity, and floating ring temperature rise are as follows:

$$\begin{cases} \sum_{i=1}^M \sum_{j=1}^N \frac{|p^{k+1} - p^k|}{|p^k|} \leq 10^{-5} \\ \left| \frac{F_g - F}{F_g} \right| < 10^{-3} \\ \left| \frac{\Delta T_R' - \Delta T_R}{\Delta T_R} \right| < 10^{-2} \end{cases} \quad (24)$$

where F_g is the external load on the journal, F is the load capacity of the inner oil film, and M and N are the number of grids.

3.2. Verification of Pressure and Static Characteristics Parameters

To validate the lubrication calculation method of the pure three-lobe structure subroutine, other interfering factors were eliminated, and the static characteristics of a typical three-lobe bearing were computed. The three-lobe bearing model was established in Dyrobes [34]. The bearing parameters were chosen in accordance with the calculation program, as illustrated in Table 1. The calculated results of both are presented in Table 2. The relative deviations of static characteristic parameters are all within 10%. Therefore, the results are in good agreement. Since this paper includes the influence of the static pressure flow and outer film, the complete calculation program was simultaneously compared with the calculation results obtained from fluid simulation software. The bearing parameters remain consistent with those outlined in Table 1, and Figure 5 displays the calculation results of the pressure distribution. Motion boundary conditions were adopted in the simulation [35], and a program written by UDFs (User-Defined Functions) simulated the movement of the journal from the center to the designated stable eccentricity position. The transient calculation was chosen due to the complexity of modeling and meshing the journal eccentricity, although such calculations are time-consuming. The temperature–viscosity curve was also implemented using UDFs and remained consistent with the program. The pressure comparison results demonstrate the accuracy of the complete calculation program presented in this paper. Furthermore, the computational efficiency of the program in this paper exceeds that of the simulation software.

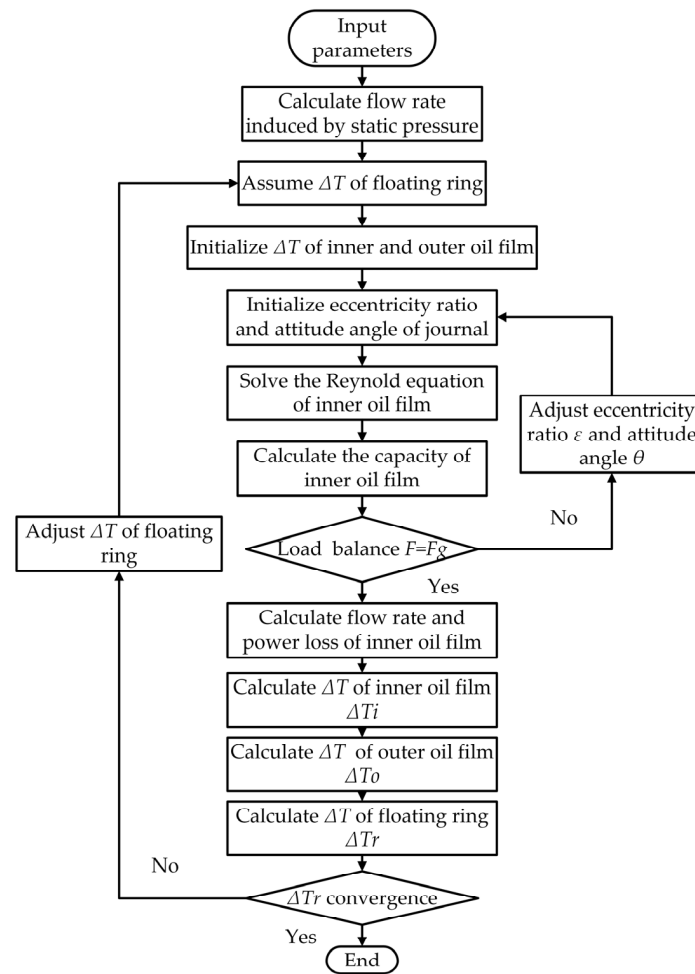


Figure 4. Flowchart of the calculation.

Table 1. Parameters of the three-lobe SFRBs.

Parameters	Value	Parameters	Value
Rotor speed ω	64,500 r/min	External load F_g	63.49 N
Oil supply pressure P_s	0.2 MPa	Preload factor m	0.8592
Bearing length L	20.2 mm	Oil-specific heat κ	2000 J/kg·°C
Radius clearance C_p	0.149148 mm	Oil density ρ	850 kg/m ³
Radius clearance C_b	0.021 mm	Heat transfer coefficient c_p	0.13 W/m·K
Rotor radius R_j	12.35 mm	Oil supply temperature T_s	50 °C
Radius of hole R_1	3 mm	Number of holes N_1	3
Radius of hole R_2	1.6 mm	Number of holes N_2	3
Surface roughness σ	0.8 μ m		

Table 2. Verification of static characteristics of typical three-lobe bearing.

Performance Parameters	Dyrobes	Present	Relative Error
Maximum pressure P_{max}/Mpa	7.8268	7.1973	8.0%
Minimum film thickness H_{min}/mm	0.02045	0.02039	0.29%
Attitude angle θ/deg	23.8	22.1	7.1%
Power loss P_f/kW	3.12451	2.98549	4.4%
Flow rate Q/lpm	1.832	2.005	9.44%
Eccentricity ratio e/C_b	0.0287	0.0310	8.0%
Viscosity $\mu/cPoise$	10.6601	9.8037	8.0%

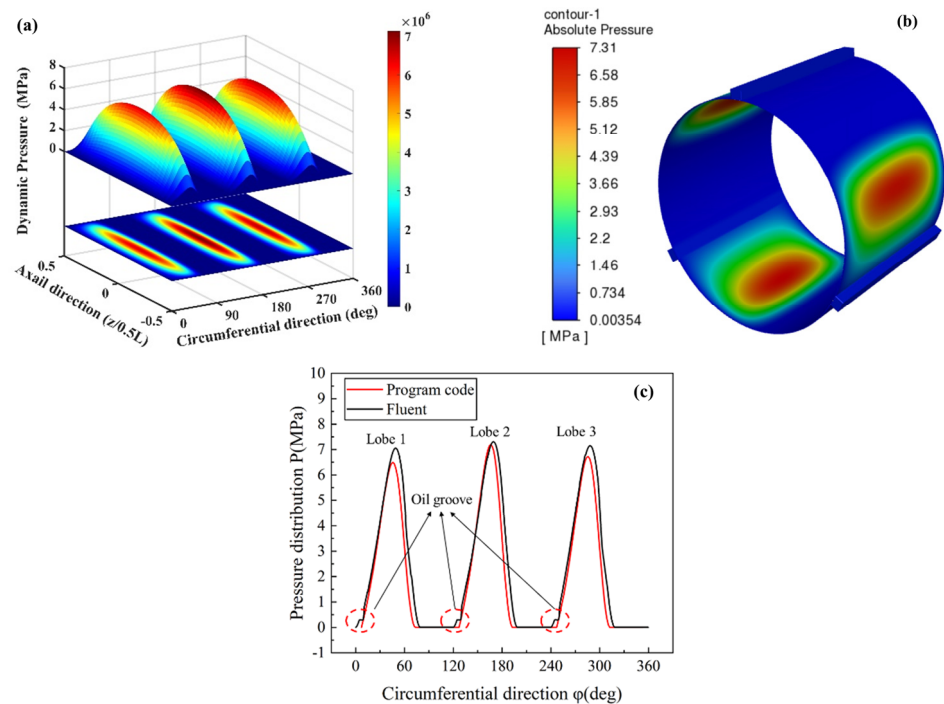


Figure 5. Validation of pressure distribution. (a) Pressure distribution by program code; (b) pressure distribution by Fluent; (c) comparison of pressure distribution on the X–Y plane.

4. Results and Discussion

4.1. Effect of Operating Parameters on the Static Characteristics

In order to analyze the static characteristics of the three-lobe SFRBs under various operating conditions, four typical operating parameters were considered in this section: journal speed, external load, oil supply pressure, and oil supply temperature. Using the THD calculation program established in this paper, the influence of these operating parameters on different lubrication static characteristics was calculated in detail. The bearing structure parameters were selected according to Table 1. When analyzing each operating parameter, the values of the others were kept unchanged to avoid interference and to clearly demonstrate the observed patterns. These operating parameters represent normal working conditions of the turbocharger, with corresponding values as follows: journal speed = 30,000 r/min, external load = 63.98 N, oil supply pressure = 2000 Pa, and oil supply temperature = 50 °C.

4.1.1. Effect of Operating Parameters on the Temperature Rise

The influence of four operating parameters on the temperature rise of the floating ring and oil film is depicted in Figure 6. As illustrated in Figure 6a, an increase in the oil supply pressure from 1.5 kPa to 5 kPa results in a decrease in the temperature rise of both the oil film and floating ring. This phenomenon can be attributed to the increase in end leakage caused by static pressure, which effectively dissipates more heat. Notably, the temperature rise of both components remains nearly the same. The external load has minimal effect on the temperature rise, as evidenced by Figure 6b. Figure 6c indicates that the influence of the oil supply temperature on the temperature rise closely resembles that of the oil supply pressure. However, the key distinction lies in the observation that, with an increase in the oil supply temperature from 30 °C to 80 °C, the temperature rise diminishes significantly. Moreover, as the oil supply temperature rises, the declining trend of the temperature rise gradually slows down, and the temperature rise amplitude of the oil film and floating ring gradually converges. Conversely, Figure 6d demonstrates an opposite trend. With an increase in speed from 10,000 r/min to 50,000 r/min, the temperature rise steadily increases. At low speeds, the temperature rise amplitude of the oil film and floating ring is minimal,

and the discrepancy between them increases with a rising speed. Additionally, it is evident that the temperature rise of the inner film is the highest, followed by the floating ring, while the outer film exhibits the lowest temperature rise. This trend persists across all operating conditions.

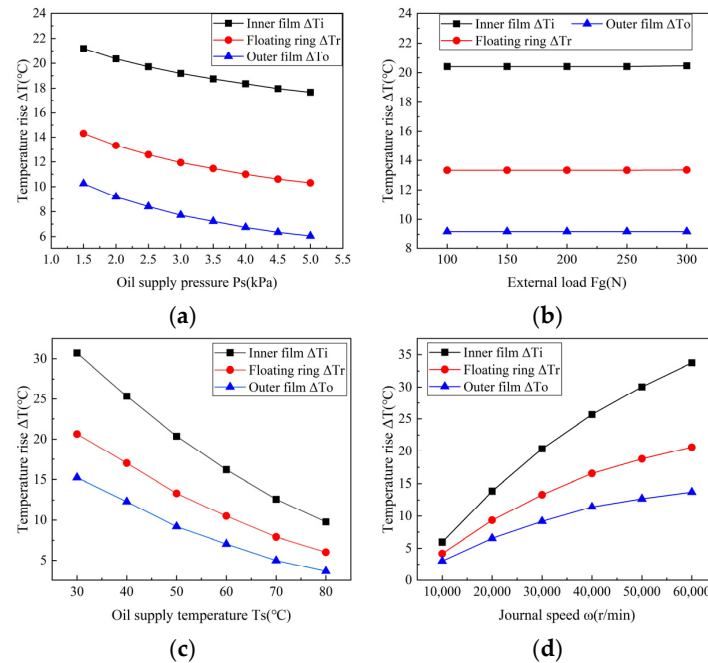


Figure 6. Influence of four typical operating parameters on temperature rise. (a) Effect by Oil supply pressure; (b) effect by External load; (c) effect by Oil supply temperature; (d) effect by Journal speed.

4.1.2. Effect of Operating Parameters on the Power Loss

Figure 7 illustrates the influence of the four operating parameters on the friction power loss of the inner film. Since the inner film of three-lobe SFRBs has a complete dynamic pressure oil film on all three lobes, friction power loss exists in each lobe, following the order depicted in Figure 2. As can be seen from Figure 7a, the friction power loss of all lobes increases with an increase in the oil supply pressure from 1.5 kPa to 5 kPa, with the power loss growth amplitude approximately 67 W. When the load increases from 100 N to 300 N, the friction power loss of lobe 2 increases linearly, while that of lobe 1 and lobe 3 decreases linearly. As depicted in Figure 7b, the total friction power loss of the inner film increases slightly. Figure 7c shows that the friction power loss of all the lobes decreases with the increase in the oil supply temperature, and within the actual oil supply temperature range of the turbocharger, the change in the oil supply temperature has a significant impact on the friction power loss. Additionally, within the actual speed range, the influence of the journal speed becomes more obvious in Figure 7d, and at the same time, the power loss of each lobe increased nearly 1 kW.

4.1.3. Effect of Operating Parameters on the End Leakage

The influence of the four operating parameters on the end leakage of the floating ring and oil film is illustrated in Figure 8. As depicted in Figure 8a, an increase in the journal speed from 10,000 r/min to 60,000 r/min results in a linear increase in the total end leakage of the inner oil film from 1.29 L/min to 2.85 L/min. Figure 8b presents the variation in the flow rate with the oil supply pressure. Notably, the increase in the oil supply pressure has little impact on the flow rate calculated by dynamic pressure, while the total flow rate increases from 1.78 L/min to 2.48 L/min. This suggests that the increase in the static pressure flow rate caused by the oil supply pressure significantly contributes to the total flow rate. This finding further underscores the importance of considering the

static pressure flow in a fluid lubrication analysis. Furthermore, whether the external load increases from 100 N to 300 N or the oil supply temperature rises from 30 °C to 80 °C, the flow rate remains almost unchanged, as depicted in Figure 8c,d. This indicates that end leakage is not sensitive to changes in external load and supply temperature.

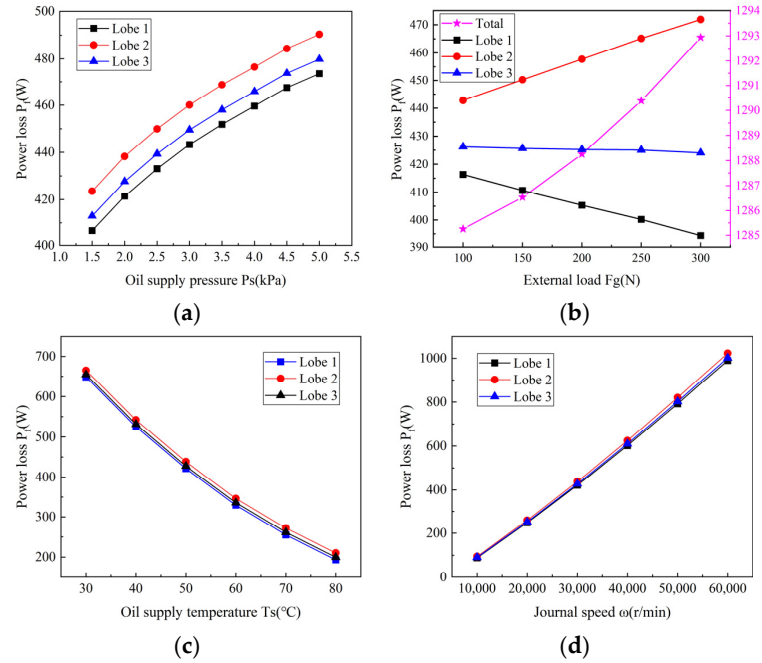


Figure 7. Influence of four typical operating parameters on power loss. (a) Effect by Oil supply pressure; (b) effect by External load; (c) effect by Oil supply temperature; (d) effect by Journal speed.

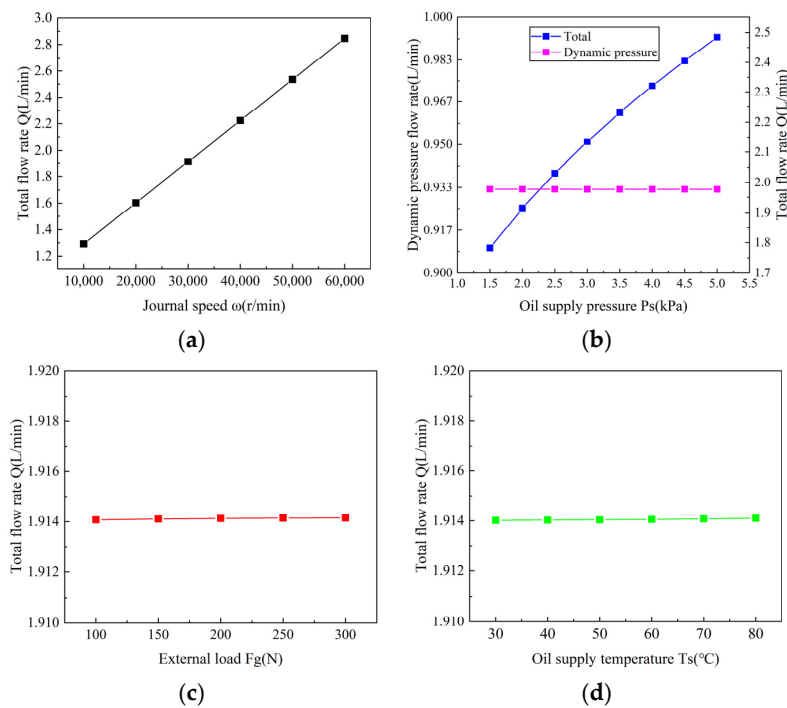


Figure 8. Influence of four typical operating parameters on flow rate. (a) Effect by Journal speed; (b) effect by Oil supply pressure, blue and pink line are total and dynamic pressure flow rate respectively; (c) effect by External load; (d) effect by Oil supply temperature.

4.1.4. Effect of Operating Parameters on Eccentricity Ratio and Attitude Angle

The impact of the four operational parameters on the eccentricity ratio and attitude angle of the journal is elucidated in Figure 9. It can be observed from Figure 9a,c that the eccentricity ratio and attitude angle decrease with the increase in the oil supply pressure and rotation speed. Moreover, the greater the oil supply pressure and rotation speed, the smaller the rate of decline. Specifically, the transition from 1.5 kPa to 5 kPa in the oil supply pressure demonstrates a relatively modest decrease in both the eccentricity ratio and attitude angle, whereas the escalation from 10,000 r/min to 60,000 r/min in rotational speed exhibits a more remarkable reduction. Additionally, Figure 9b,d illustrates that the eccentricity ratio and attitude angle exhibit an upward trend with elevating oil supply temperature and load. Notably, these parameters demonstrate nonlinear changes concerning the oil supply temperature while displaying an approximately linear relationship with load. Furthermore, it is noteworthy to observe from the results depicted in Figure 9 that as the eccentricity diminishes, there is a corresponding decrease in the attitude angle. This behavior stands in contrast to that observed in circular bearings, underscoring the superior centripetal effect exhibited by the journal of three-lobe SFRBs. Moreover, the presence of oil film on the tiles on both sides contributes significantly to the overall stability of the bearing system.

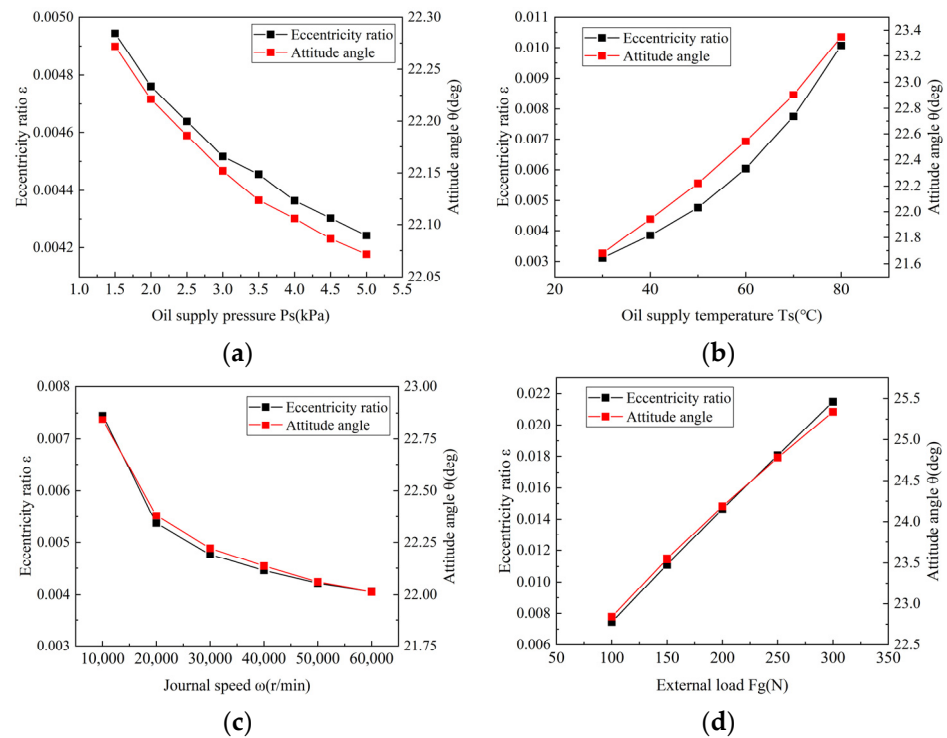


Figure 9. Influence of four operating parameters on eccentricity ratio and attitude angle. (a) Effect by Oil supply pressure; (b) effect by Oil supply temperature; (c) effect by Journal speed; (d) effect by External load.

4.1.5. Effect of Operating Parameters on the Maximum Film Pressure

Figure 10 illustrates the impact of four operating parameters on the maximum oil film pressure of the inner oil film. As depicted in Figure 10a, with an increase in the oil supply pressure from 1500 Pa to 5000 Pa, the maximum oil film pressure experiences a gradual increase on lobes 1 and 3 while displaying a slight decrease on lobe 2. Notably, the oil supply pressure exhibits a slight influence on the maximum oil film pressure. Turning to Figure 10b, the influence of external load on the maximum oil film pressure is evident. As the external load increases, the maximum oil film pressure exhibits a linear increase on lobe 2 while demonstrating a linear decrease on lobes 1 and 3. In Figure 10c, it can be observed that the maximum oil film pressure on all three lobes decreases with an increase in the oil

supply temperature, with the amplitude of change diminishing as the temperature rises. Lastly, in Figure 10d, the maximum oil film pressure of the three lobes demonstrates a linear increase with the increase in the journal speed.

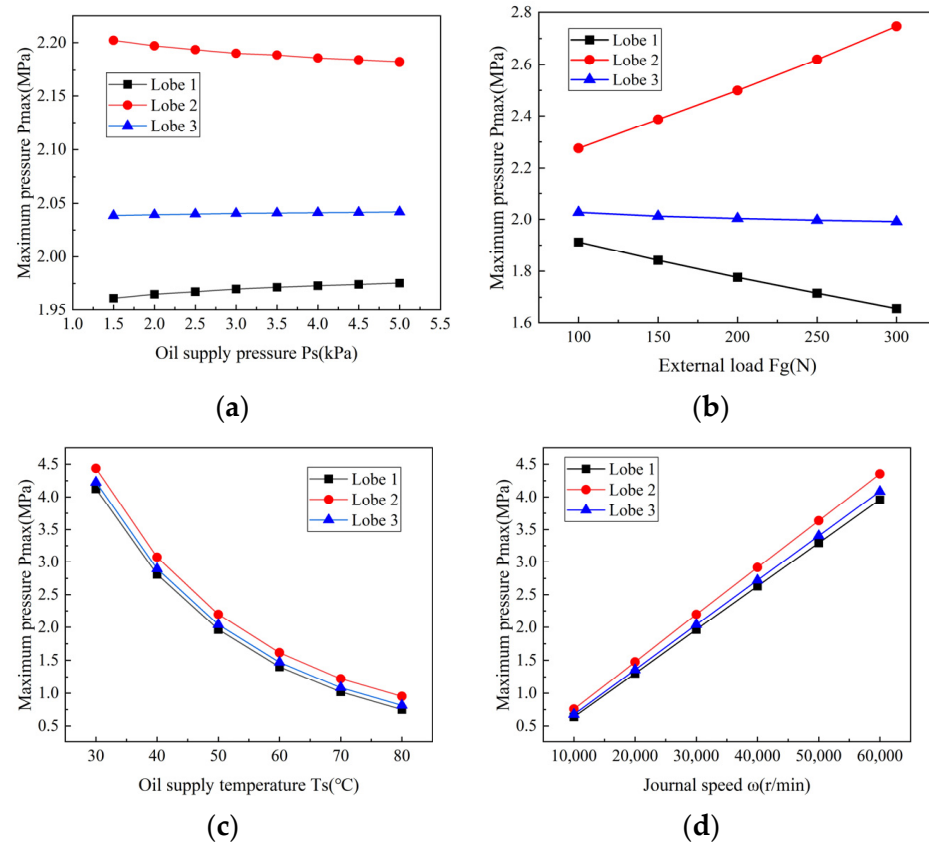


Figure 10. Influence of four typical operating parameters on maximum pressure. (a) Effect by Oil supply pressure; (b) effect by External load; (c) effect by Oil supply temperature; (d) effect by Journal speed.

4.1.6. Effect of Operating Parameters on the Minimum Film Thickness

Figure 11 illustrates the influence of the four operating parameters on the minimum oil film thickness of the inner oil film. As depicted in Figure 11a, an increase in the oil supply pressure results in a decrease in the minimum oil film thickness on lobes 1 and 3, while an increase is observed on lobe 2. The effect of the external load on the minimum film thickness corresponds to the maximum oil film pressure; that is, the maximum oil film pressure coincides with the minimum oil film thickness, as evidenced by Figure 11b. In Figure 11c, it is shown that an increase in the oil supply temperature leads to an increase in the minimum oil film thickness of lobes 1 and 3, while a decrease is observed on lobe 2. Conversely, the effect of the journal speed on the minimum film thickness is opposite to that of the oil supply temperature, as depicted in Figure 11d. Additionally, it is noteworthy that the minimum oil film thickness of lobe 2 consistently remains the lowest, indicating that lobe 2 bears the primary bearing capacity, consistent with the observation of the maximum oil film pressure.

4.2. Effect of Operating Parameters on the Dynamic Characteristics

In order to analyze the dynamic characteristics of three-lobe SFRBs under different operating conditions, the coupling effect of three significant operating parameters on the stiffness and damping coefficients was analyzed in this section. The selection of bearing structure parameters in the calculation is the same as those in the static characteristic analysis.

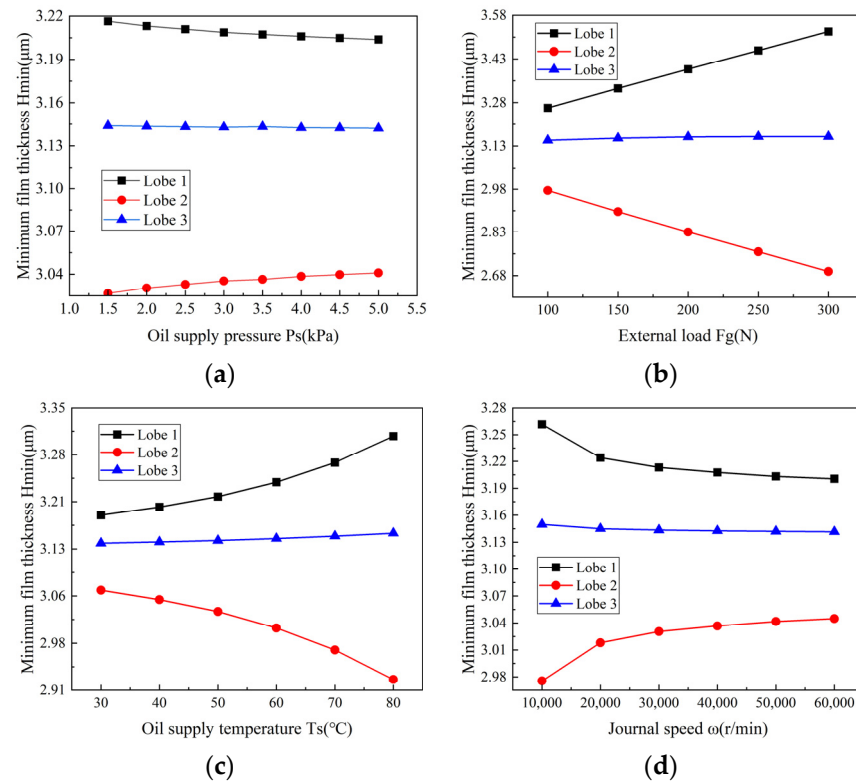


Figure 11. Influence of four typical operating parameters on minimum film thickness. (a) Effect by Oil supply pressure; (b) effect by External load; (c) effect by Oil supply temperature; (d) effect by Journal speed.

4.2.1. Coupling Effect on the Stiffness Coefficients

The variations in the stiffness coefficients of three-lobe SFRBs under different oil supply temperatures versus journal speed are depicted in Figure 12. In Figure 12a, the direct stiffness K_{xx} increases in the negative direction of x . With the increase in the journal speed, the direct stiffness K_{xx} exhibits more nonlinearity at low supply temperatures and journal speeds. For the same speed, the higher the oil supply temperature, the smaller the amplitude of the direct stiffness K_{xx} . In Figure 12b, the direct stiffness K_{yy} presents negative values in the Y direction at low speeds; when the speed exceeds a certain value, K_{yy} becomes positive in the Y direction. Interestingly, when the oil supply temperature is 50°C , the direct stiffness K_{yy} increases with increasing speed until it reaches 30,000 r/min and then decreases. The results of the cross stiffness K_{xy} are shown in Figure 12c. The amplitude of K_{xy} in the negative x direction increases with the increase in the journal speed and decreases when the journal speed exceeds a certain value. Moreover, the greater the oil supply temperature, the higher the critical speed. Lower supply temperatures and higher journal speeds result in greater cross stiffness K_{yx} , as depicted in Figure 12d.

The variation in the stiffness coefficients of three-lobe SFRBs under different oil supply pressures versus journal speed is shown in Figure 13. In Figure 13a, the amplitude of the direct stiffness K_{xx} in the negative direction of x increases with an increase in speed, while the slope of the curve decreases as the oil supply pressure increases. In Figure 13b, the amplitude of the direct stiffness K_{yy} first increases and then decreases with an increase in speed. At the same time, it can be clearly seen that the oil supply pressure has a significant effect on the change in K_{yy} , especially at a high speed. In Figure 13c, the oil supply pressure presents an opposite effect on the cross stiffness K_{xy} at different speed ranges. Moreover, the cross stiffness K_{yx} increases slightly with the increase in the oil supply pressure, as shown in Figure 13d.

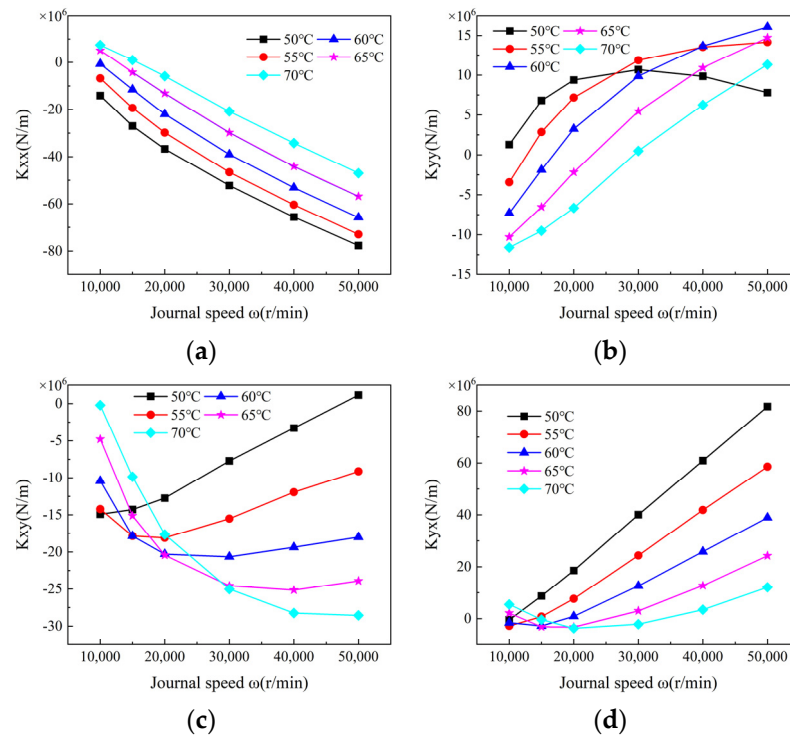


Figure 12. Effect of oil supply temperature versus speed on the stiffness coefficients. (a) Direct stiffness coefficient K_{xx} ; (b) direct stiffness coefficient K_{yy} ; (c) cross stiffness coefficient K_{xy} ; (d) cross stiffness coefficient K_{yx} .

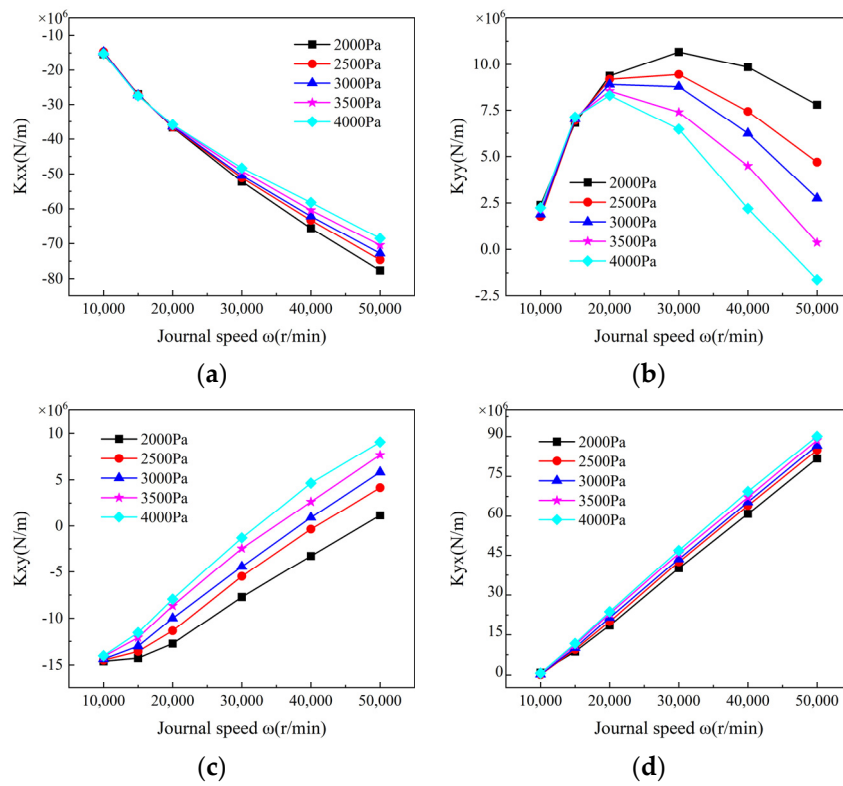


Figure 13. Effect of oil supply pressure versus speed on the stiffness coefficients. (a) Direct stiffness coefficient K_{xx} ; (b) direct stiffness coefficient K_{yy} ; (c) cross stiffness coefficient K_{xy} ; (d) cross stiffness coefficient K_{yx} .

4.2.2. Coupling Effect on the Damping Coefficients

The variation in the damping coefficients of three-lobe SFRBs under different oil supply temperatures versus journal speed is shown in Figure 14. In Figure 14a, the amplitude of the main damping coefficient C_{xx} initially increases with speed and then tends to remain unchanged. However, it decreases slightly when the oil supply temperature is 50 °C, 55 °C, and 60 °C. A higher supply temperature causes a smaller C_{xx} . In Figure 14b, the main damping coefficient C_{yy} decreases remarkably with an increase in the oil supply temperature, particularly in the high-speed zone. At lower oil supply temperatures, C_{yy} tends to increase, while at higher oil supply temperatures, it decreases and stabilizes. The variations in the cross damping coefficients are depicted in Figure 14c,d. It can be observed that the oil supply temperature has a great impact on cross damping C_{xy} and C_{yx} , especially at speeds below 20,000 r/min.

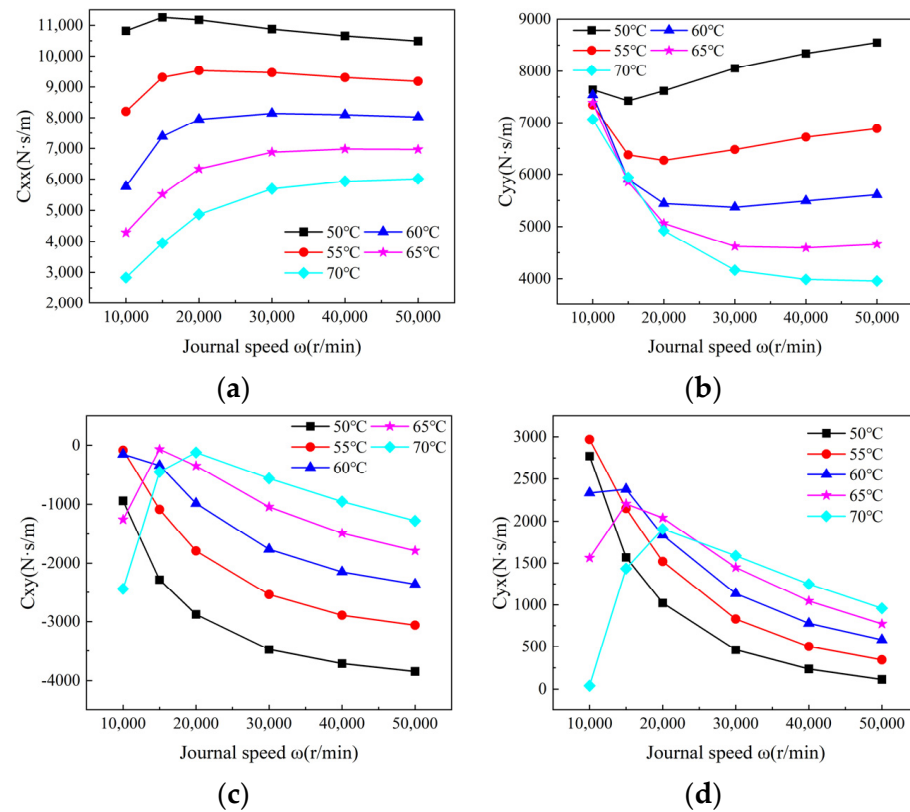


Figure 14. Effect of oil supply temperature versus speed on the damping coefficients. (a) Direct damping coefficient C_{xx} ; (b) direct damping coefficient C_{yy} ; (c) cross damping coefficient C_{xy} ; (d) cross damping coefficient C_{yx} .

The variations in the damping coefficients of three-lobe SFRBs under different oil supply pressures versus journal speed are illustrated in Figure 15. Based on Figure 15a,b, the main damping coefficient C_{xx} first increases and then decreases with speed, while C_{yy} shows the opposite trend with speed, both of which have extreme values around 15,000 r/min. The larger the oil supply pressure and the higher the journal speed, the smaller C_{xx} and the larger C_{yy} become. Oil supply pressure notably affects C_{xx} and C_{yy} at high speeds. Additionally, as can be seen from Figure 15c,d, increasing the oil supply pressure slightly reduces the amplitude of C_{yx} while slightly increasing the amplitude of C_{xy} .

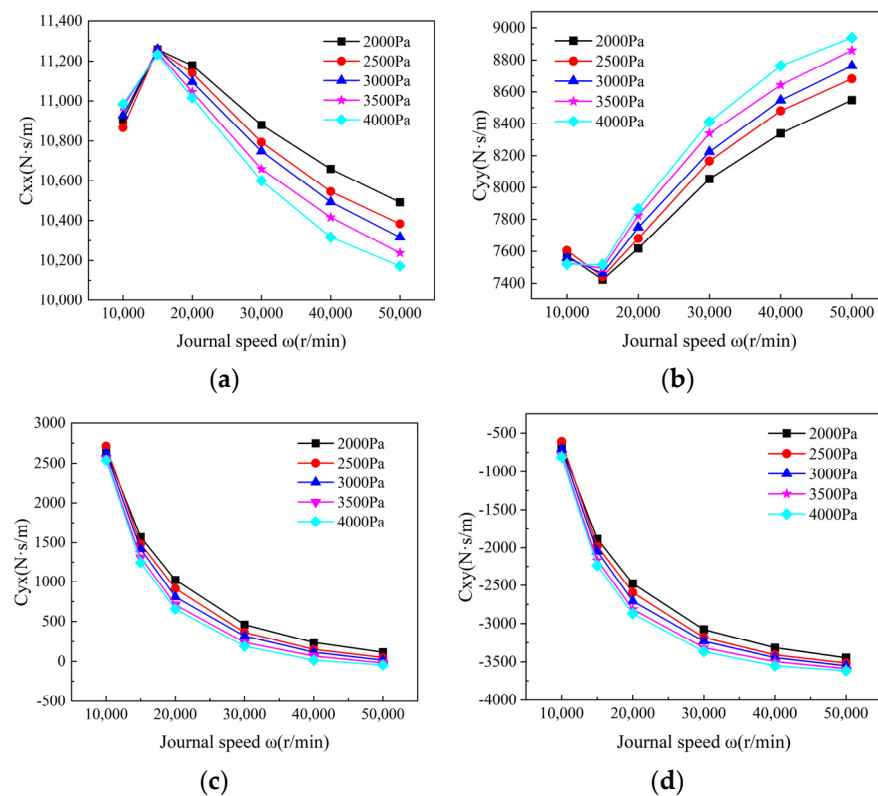


Figure 15. Effect of oil supply pressure versus speed on the damping coefficients. (a) Direct damping coefficient C_{xx} ; (b) Direct damping coefficient C_{yy} ; (c) Cross damping coefficient C_{yx} ; (d) Cross damping coefficient C_{xy} .

5. Conclusions

In this paper, a steady-state THD lubrication model was developed for three-lobe SFRBs, accounting for the temperature–viscosity effect and the static pressure flow induced by the oil supply pressure. Utilizing the FDM and the Newton–Raphson iterative procedure, the effects of the journal speed, external load, oil supply pressure, and oil supply temperature on the static characteristics of the SFRBs were individually computed. Furthermore, the coupling effect of three typical operating parameters on the dynamic characteristics was investigated. The conclusions drawn are as follows:

1. The results of the static characteristic calculations indicate that the oil supply pressure should not be disregarded in end leakage computations. With an increasing oil supply pressure and oil supply temperature, the temperature rise and maximum oil film pressure of the three-lobe SFRBs gradually decrease, while the oil film thickness gradually increases. This implies a more uniform bearing capacity across the three lobes and an enhancement in the lubrication state of the bearing. However, higher oil supply pressure also leads to increased friction power loss. The end leakage exhibits insensitivity to changes in the external load and oil supply temperature.
2. Within the three-lobe SFRBs, the maximum oil film pressure and minimum oil film thickness consistently occur in lobe 2, corresponding to the bottom tile. This suggests that lobe 2 bears the primary load and is most susceptible to wall friction.
3. The stiffness and damping of three-lobe SFRBs exhibit obvious nonlinear characteristics across the actual speed range. Additionally, the oil supply temperature significantly alters the trend of stiffness and damping, whereas the oil supply pressure has less influence on them, particularly on the damping coefficients.

Author Contributions: Methodology, J.D.; software, J.D.; validation, J.D. and C.Z.; formal analysis, J.G.; supervision, J.G.; writing—original draft preparation, J.D.; writing—review and editing, J.Z. and H.W. All authors have read and agreed to the published version of the manuscript.

Funding: This research received no external funding.

Data Availability Statement: The original contributions presented in the study are included in the article, further inquiries can be directed to the corresponding author.

Conflicts of Interest: Chen Zong was employed by Chongqing Jiangjin Shipbuilding Industry Co., Ltd. The remaining authors declare that the research was conducted in the absence of any commercial or financial relationships that could be construed as a potential conflict of interest.

Nomenclature

A_i, A_r, A_o	Heat transfer area of inner oil film, floating ring, outer oil film
A_{ie}, A_{oe}	Area of inner film flank, outer film flank
C_p	Radius clearance of lobe
C_b	Radius clearance of bearing
cp	Heat transfer coefficient
$C_{ee}, C_{e\theta}, C_{\theta\theta}, C_{\theta e}$	Damping coefficients under $e - \theta$ coordinates
$C_{xx}, C_{xy}, C_{yx}, C_{yy}$	Damping coefficients under X–Y coordinates
e	Eccentricity of journal
F, Fg	Oil film load capacity, external load
h, h_{min}	Oil film thickness, minimum film thickness
h_{wi}, h_{wo}	Pressure loss of inner film, outer film
$K_{ee}, K_{e\theta}, K_{\theta\theta}, K_{\theta e}$	Stiffness coefficients under $e - \theta$ coordinates
$K_{xx}, K_{xy}, K_{yx}, K_{yy}$	Stiffness coefficients under X–Y coordinates
m	Preload factor
$N1, N2$	Number of holes on floating ring, on bushing
P, P_{max}	Pressure, maximum pressure
$P_e, P_\theta, P'_e, P'_\theta$	Disturbance pressure
P_f	Power loss based on dynamic pressure equation
P_i, P_o, P_s	Pressure of inlet on floating ring, on bushing, supply pressure
$Q, Q_i, Q_o, Q_{i1}, Q_{i2}$	Flow rate, flow rate of inner film, outer film, dynamic pressure flow rate of inner film, static pressure flow rate of inner film
$R_j, R1, R2$	Journal radius, radius of hole on floating ring, on bushing
$T_s, \Delta T_i, \Delta T_o, \Delta T_r$	Supply oil temperature, temperature rise of inner film, outer film, ring
U_j	Journal linear velocity
α	Lobe sequence number, $\alpha = 1, 2, 3$
β	Cover angle of lobe
ε	Journal eccentricity ratio
θ	Attitude angle
κ	Oil specific heat
λ_p	Pressure loss coefficient
μ	Oil viscosity
ρ	Oil density
ω	Journal rotation speed

Appendix A

The Reynolds equation of the SFRBs was solved by the half-step FDM, and the oil film grid division is shown in Figure A1. The dimensionless Reynolds equation is as follows:

$$\frac{\partial}{\partial \varphi} \left(H_\alpha^3 \frac{\partial p_\alpha}{\partial \varphi} \right) + \frac{\partial}{\partial \lambda} \left(H_\alpha^3 \frac{\partial p_\alpha}{\partial \lambda} \right) = 2 \frac{\partial H_\alpha}{\partial \varphi}$$

The dimensionless parameters are defined as $\lambda = 2z/L$ ($-1 \leq \lambda \leq 1$), $H_\alpha = h_\alpha/C_p$, $p_\alpha = P_\alpha \psi^2/6\mu\omega$, and $\psi = C_p/R_j$. Then, the discretized Reynolds equation on each lobe is as follows:

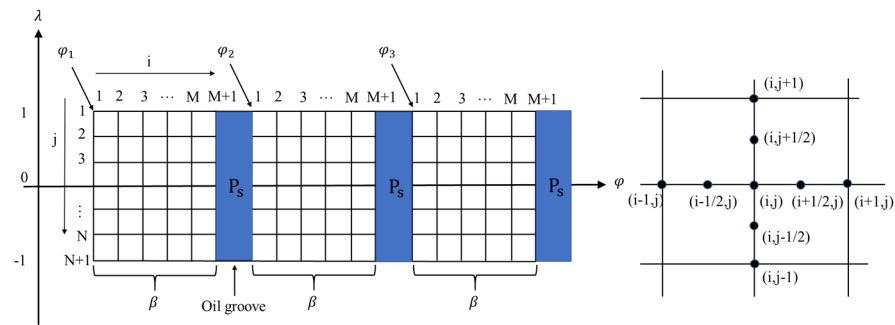


Figure A1. Mesh of inner oil film.

$$A_{i,j}^{\alpha} P_{i+1,j}^{\alpha} + B_{i,j}^{\alpha} P_{i-1,j}^{\alpha} + C_{i,j}^{\alpha} P_{i,j+1}^{\alpha} + D_{i,j}^{\alpha} P_{i,j-1}^{\alpha} - E_{i,j}^{\alpha} P_{i,j}^{\alpha} = F_{i,j}^{\alpha}$$

The difference coefficient can be summarized as

$$A_{i,j}^{\alpha} = \frac{(H_{\alpha}^3)_{i+1/2,j}}{\Delta\varphi^2}, \quad B_{i,j}^{\alpha} = \frac{(H_{\alpha}^3)_{i-1/2,j}}{\Delta\varphi^2},$$

$$C_{i,j}^{\alpha} = \left(\frac{4R_j^2}{L^2}\right) \frac{(H_{\alpha}^3)_{i,j+1/2}}{\Delta\lambda^2}, \quad D_{i,j}^{\alpha} = \left(\frac{4R_j^2}{L^2}\right) \frac{(H_{\alpha}^3)_{i,j-1/2}}{\Delta\lambda^2},$$

$$E_{i,j}^{\alpha} = A_{i,j}^{\alpha} + B_{i,j}^{\alpha} + C_{i,j}^{\alpha} + D_{i,j}^{\alpha}$$

$$F_{i,j}^{\alpha} = 2\Delta\varphi \left((H_{\alpha})_{i+1/2,j} - (H_{\alpha})_{i-1/2,j} \right)$$

The Newton–Raphson method was used to adjust the temperature rise in the floating ring, and it can be described as follows:

$$\Delta T_r^{n+1} = \Delta T_r^n - \frac{f(\Delta T_r^n)}{f'(\Delta T_r^n)}$$

where $f(\Delta T_r^n) = (\gamma\Delta T_i^n + \zeta\Delta T_o^n - (\gamma + \zeta)\Delta T_r^n)$, $f'(\Delta T_r^n) = -(\gamma + \zeta)$. The subscript n represents the number of iterations, and γ and ζ are coefficients in Equation (7), $\gamma = A_i H_i$, $\zeta = A_o H_o$.

References

- Kirk, R.G. Experimental Evaluation of Hydrodynamic Bearings for a High Speed Turbocharger. *J. Eng. Gas Turbines Power* **2014**, *136*, 072501. [\[CrossRef\]](#)
- Zhang, Y.; Wang, W.; Wei, D.G.; Wang, G.; Xu, J.M.; Liu, K. Coupling analysis of tribological and dynamical behavior for a thermal turbulent fluid lubricated floating ring bearing-rotor system at ultra-high speeds. *Tribol. Int.* **2022**, *165*, 107325. [\[CrossRef\]](#)
- Tian, L.; Wang, W.J.; Peng, Z.J. Nonlinear effects of unbalance in the rotor-floating ring bearing system of turbochargers. *Mech. Syst. Signal Process.* **2013**, *34*, 298–320. [\[CrossRef\]](#)
- Eling, R.; Te Wierik, M.; Van Ostayen, R.; Rixen, D. Rotordynamic and Friction Loss Measurements on a High Speed Laval Rotor Supported by Floating Ring Bearings. *Lubricants* **2017**, *5*, 7. [\[CrossRef\]](#)
- Cao, J.; Dousti, S.; Allaire, P.; Dimond, T. Nonlinear Transient Modeling and Design of Turbocharger Rotor/Semi-Floating Bush Bearing System. *Lubricants* **2017**, *5*, 16. [\[CrossRef\]](#)
- Zhang, Y.; Wang, W.; Wei, D.; Wang, G.; Xu, J.; Liu, K. Dynamic stability of unbalance-induced vibration in a turbocharger rotor-bearing system with the nonlinear effect of thermal turbulent lubricating fluid film. *J. Sound Vib.* **2022**, *528*, 116909. [\[CrossRef\]](#)
- Chen, W.J. Rotordynamics and bearing design of turbochargers. *Mech. Syst. Signal Process.* **2012**, *29*, 77–89. [\[CrossRef\]](#)
- Schweizer, B. Dynamics and stability of turbocharger rotors. *Arch. Appl. Mech.* **2009**, *80*, 1017–1043. [\[CrossRef\]](#)
- Orcutt, F.K.; Ng, C.W. Steady-State and Dynamic Properties of the Floating-Ring Journal Bearing. *J. Lubr. Technol.* **1968**, *90*, 243–253. [\[CrossRef\]](#)
- Nikolajsen, J.L. The Effect of Variable Viscosity on the Stability of Plain Journal Bearings and Floating-Ring Journal Bearings. *J. Lubr. Technol.* **1973**, *95*, 447–456. [\[CrossRef\]](#)
- Mokhtar, M.O.A. Floating ring journal bearings: Theory, design and optimization. *Tribol. Int.* **1981**, *14*, 113–119. [\[CrossRef\]](#)
- Li, C.-H.; Rohde, S.M. On The Steady State and Dynamic Performance Characteristics of Floating Ring Bearings. *J. Lubr. Technol.* **1981**, *103*, 389–397. [\[CrossRef\]](#)

13. Clarke, D.M.; Fall, C.; Hayden, G.N.; Wilkinson, T.S. A Steady-State Model of a Floating Ring Bearing, Including Thermal Effects. *J. Tribol.* **1992**, *114*, 141–149. [[CrossRef](#)]
14. Jung, W.; San Andres, L.; Kim, J. A Nonlinear Rotordynamics Model for Automotive Turbochargers Coupled to a Physical Model for A (Semi) Floating Ring Bearing System. *J. Eng. Gas Turbines Power* **2022**, *144*, 111002. [[CrossRef](#)]
15. San Andrés, L.; Jung, W.; Hong, S.-K. A Thermo-Hydrodynamic Model for Thermal Energy Flow Management in A (Semi) Floating Ring Bearing System for Automotive Turbochargers. *J. Eng. Gas Turbines Power* **2021**, *143*, 011013. [[CrossRef](#)]
16. San Andrés, L.; Yu, F.; Gjika, K. On the Influence of Lubricant Supply Conditions and Bearing Configuration to the Performance of (Semi) Floating Ring Bearing Systems for Turbochargers. *J. Eng. Gas Turbines Power* **2017**, *140*, 032503. [[CrossRef](#)]
17. Gjika, K.; San Andrés, L.; Larue, G.D. Nonlinear Dynamic Behavior of Turbocharger Rotor-Bearing Systems with Hydrodynamic Oil Film and Squeeze Film Damper in Series: Prediction and Experiment. *J. Comput. Nonlin. Dyn.* **2010**, *5*, 041006. [[CrossRef](#)]
18. Andres, L.S.; Rivadeneira, J.C.; Gjika, K.; Groves, C.; LaRue, G. Rotordynamics of small turbochargers supported on floating ring bearings—Highlights in bearing analysis and experimental validation. *J. Tribol. T Asme* **2007**, *129*, 391–397. [[CrossRef](#)]
19. Andrés, L.S.; Rivadeneira, J.C.; Gjika, K.; Groves, C.; LaRue, G. A Virtual Tool for Prediction of Turbocharger Nonlinear Dynamic Response: Validation Against Test Data. *J. Eng. Gas Turbines Power* **2006**, *129*, 1035–1046. [[CrossRef](#)]
20. Duan, W.; Chu, F.; Kim, C.-H.; Lee, Y.-B. A bulk-flow analysis of static and dynamic characteristics of floating ring seals. *Tribol. Int.* **2007**, *40*, 470–478. [[CrossRef](#)]
21. Pei, S.; Xu, H.; Yun, M.; Shi, F.; Hong, J. Effects of surface texture on the lubrication performance of the floating ring bearing. *Tribol. Int.* **2016**, *102*, 143–153. [[CrossRef](#)]
22. Wang, X.; Li, H.; Lu, W.; Meng, G. Stiffness and Damping Properties of (Semi) Floating Ring Bearing Using Magnetorheological Fluids as Lubricant. *J. Tribol.* **2017**, *139*, 051701. [[CrossRef](#)]
23. Guo, H.; Yang, S.; Zhang, S.; Zhang, Z. Influence of temperature–viscosity effect on ring-journal speed ratio and stability for a hydrodynamic floating ring bearing. *Ind. Lubr. Tribol.* **2019**, *71*, 540–547. [[CrossRef](#)]
24. Zhang, C.; Men, R.; Wang, Y.; He, H.; Chen, W. Experimental and numerical investigation on thermodynamic performance of full-floating ring bearings with circumferential oil groove. *Proc. Inst. Mech. Eng. Part J J. Eng. Tribol.* **2019**, *233*, 1182–1196. [[CrossRef](#)]
25. Dyk, Š.; Smolík, L.; Rendl, J. Predictive capability of various linearization approaches for floating-ring bearings in nonlinear dynamics of turbochargers. *Mech. Mach. Theory* **2020**, *149*, 103843. [[CrossRef](#)]
26. Yang, S.; Guo, H.; Zhang, S.-L.; Xia, B.-Q. Thermohydrodynamic Characteristics and Stability Analysis for a Journal Hybrid Floating Ring Bearing within Laminar and Turbulent Mixed Flow Regime. *J. Tribol.* **2020**, *143*, 031801. [[CrossRef](#)]
27. Ziese, C.; Irmscher, C.; Nitzschke, S.; Daniel, C.; Woschke, E.; Klimpel, T. Influence of Lubricant Film Cavitation on the Vibration Behavior of a Semifloating Ring Supported Turbocharger Rotor with Thrust Bearing. *J. Eng. Gas Turbines Power* **2022**, *144*, 041014. [[CrossRef](#)]
28. Xie, Z.; Zhu, W. An investigation on the lubrication characteristics of floating ring bearing with consideration of multi-coupling factors. *Mech. Syst. Signal Process.* **2022**, *162*, 108086. [[CrossRef](#)]
29. Soni, S.; Vakharia, D. Dynamic performance analysis of a noncircular cylindrical floating ring bearing. *Proc. Inst. Mech. Eng. Part J J. Eng. Tribol.* **2017**, *231*, 745–765. [[CrossRef](#)]
30. Soni, S.; Vakharia, D. A steady-state performance analysis of a non-circular cylindrical floating ring journal bearing. *Proc. Inst. Mech. Eng. Part J J. Eng. Tribol.* **2017**, *231*, 41–56. [[CrossRef](#)]
31. Zhang, C.; Wang, Y.; Men, R.; He, H.; Chen, W. The effect of three-lobed bearing shapes in floating-ring bearings on the nonlinear oscillations of high-speed rotors. *Proc. Inst. Mech. Eng. Part J J. Eng. Tribol.* **2020**, *234*, 751–769. [[CrossRef](#)]
32. Zhang, C.; Wang, Y.; Men, R.; He, H.; Chen, W. Dynamic behaviors of a high-speed turbocharger rotor on elliptical floating-ring bearings. *Proc. Inst. Mech. Eng. Part J J. Eng. Tribol.* **2019**, *233*, 1785–1799. [[CrossRef](#)]
33. San Andrés, L.; Kerth, J. Thermal effects on the performance of floating ring bearings for turbochargers. *Proc. Inst. Mech. Eng. Part J J. Eng. Tribol.* **2004**, *218*, 437–450. [[CrossRef](#)]
34. User Manuals of Fluent. Available online: https://ansyshelp.ansys.com/account/secured?returnurl=/Views/Secured/prod_page.html?pn=Fluent&pid=Fluent&lang=en (accessed on 3 April 2024).
35. User Manuals and Documentation of Dyrobes. Available online: <https://dyrobes.com/features/user-manuals/> (accessed on 3 April 2024).

Disclaimer/Publisher’s Note: The statements, opinions and data contained in all publications are solely those of the individual author(s) and contributor(s) and not of MDPI and/or the editor(s). MDPI and/or the editor(s) disclaim responsibility for any injury to people or property resulting from any ideas, methods, instructions or products referred to in the content.